Geodesy and Geodynamics 11 (2020) 85–96

Contents lists available at ScienceDirect

Geodesy and Geodynamics

journal homepage: http://www.keaipublishing.com/geog

A numerical model for the gravimetric recovery of sub-lithospheric mantle structures

Robert Tenzer

The Department of Land Surveying and Geo-Informatics, The Hong Kong Polytechnic University, 181 Chatham Road South, Hong Kong, China

ARTICLE INFO

Article history:
Received 6 June 2019
Accepted 19 September 2019
Available online 19 November 2019

Keywords:
Asthenosphere
Crust
Gravity field
Lithosphere
Mantle

ABSTRACT

It is a well-known fact that the long-wavelength terrestrial geoid undulations are mainly attributed to deep mantle density heterogeneities, while more detailed features in the geoid geometry are associated with the topography and the lithospheric density structure. To enhance a gravitational signature of mantle density heterogeneities below the lithosphere, the gravitational contributions of topography and lithospheric density heterogeneities should be modelled and subsequently removed from Earth's gravity field. The refined gravity field obtained after this numerical procedure is more suitable for a recovery of a mantle density structure (below the lithosphere). Following this idea, methods for a spherical harmonic analysis and synthesis of gravity field and lithospheric density structures are presented, and a theoretical relation between gravity field and mass density structure is formulated. Since a gravimetric recovery of inner density structure has a non-unique solution, we propose an alternative method based on a conversion of seismic velocities to mass densities. A forward modelling approach is then employed to find the mantle density configuration that generates the gravitational field that best approximates the corresponding refined gravitational field obtained from observed gravity field after subtracting the gravitational signal of the lithosphere.

1. Introduction

Seismic velocities are primarily used to investigate density structure inside the Earth based on an adopted velocity-to-density function. Several functional relations were developed and applied for this purpose. For densities of crustal rocks located in depths exceeding 5 km, the formulae developed by Sobolev and Babeyko [1] or Christensen and Mooney [2] can be applied that takes into consideration *in situ* temperature and pressure conditions. Deeper in the mantle lithosphere, the conversion of seismic velocities to densities could be done based on the formula developed by Lachenbruch and Morgan [3], which takes into account the dependence of density on temperature through the coefficient of thermal expansion. With the accumulation of experimental data bearing on physical behaviors of rocks and minerals at high pressure and temperature, it becomes possible to examine the relations between seismic velocities and densities deeper in the mantle. Birch [4,5], proposed a linear relation between the velocity of compressional waves and the density for rocks and minerals with the mean atomic weight of 20–22. Later, various formulae for estimating the rock densities were developed and applied. For more information, we refer readers to [6–11].

The rock density variations typically decrease with depth, making a deep density structure more homogeneous. The first models of Earth's mantle assume a spherically symmetric density composition with density increasing with depth. From the early 1980s, images of Earth's interior provided by seismic tomography have revealed more complex structural density heterogeneities within the mantle as expected when taking into consideration the long-wavelength geoidal undulations that globally vary within ±100 m. The most significant density heterogeneities are probably related to mantle flow pattern with the most prominent two Large Low Shear Velocity Provinces (LLSVPs) at the base of the mantle

E-mail address: robert.tenzer@polyu.edu.hk.

Peer review under responsibility of Institute of Seismology, China Earthquake Administration.

Production and Hosting by Elsevier on behalf of KeAi

https://doi.org/10.1016/j.geog.2019.09.003

located beneath Africa and the Pacific (i.e. African and South Pacific super-swells). In the recent study based on the tidal tomography, Lau et al. [12] estimated that relative density variations within these formations are about 0.5%. Large density anomalies are also associated with mantle plumes under Iceland, Hawaii, Azores, and elsewhere [13]. Moreover, results of seismic tomography revealed relatively significant density variations and density discontinuities in the mantle transition zone at depths approximately between 410 and 660 km [14,15], as well as within the whole mantle.

As stated above, the mantle density structure is typically modeled from tomographic data based on a conversion of seismic velocities to mass densities. Nevertheless, additional constraining information including gravity data [16] is needed because the propagation of seismic velocities within the mantle depends mainly on rheological properties rather than density itself. An alternative method for recovering the inner density structure is to apply a gravity inversion. The main reason is that any changes in density directly propagate to changes in gravity field. However, the recovery of inner density structure from gravity data is a non-unique problem, meaning that infinity many density configurations could be assigned to just one gravity field solution. In this case, the gravimetric inversion has to be constrained using seismic data and eventually also additional geophysical, geochemical, or geodynamic information. Another aspect closely related to a gravimetric recovery of unknown (and sought) density structure or density interface below the lithosphere is a treatment of the gravitational signal of density heterogeneities within the lithosphere that should be removed from gravity field in prior of a gravity inversion. Spectral decomposition or filtering techniques are typically used for this purpose. However, the results of such procedures are not fully realistic, because the lithospheric density heterogeneities affect also a long-wavelength gravity spectrum. This makes a realistic separation of gravitational signals from different depth sources difficult. The gravitational signal of lithospheric density structures could be modelled and subsequently removed from gravity data based on applying methods for a gravimetric forward modelling of these density structures. This refined gravity field is then used to recover a density structure in the mantle below the lithosphere.

In this study, we review spectral expressions for a gravimetric forward modelling of the lithospheric density structure (section 2) that are applied in order to reveal a gravitational signature of deeper mantle density heterogeneities. We introduce spectral expressions that define the mantle density model (below the lithosphere) in terms of volumetric mass density layers (section 3). We then establish a functional relation between gravity field and density structure (section 4) based on employing a conversion of seismic velocities to mass densities (section 5). Finally, we discuss and summarize major theoretical aspects (section 6). We note that a numerical realization (due to its complexity) is out of the scope of this study.

2. Forward modelling

To recover a gravitational signature of mantle density heterogeneities below the lithosphere, corrections are applied to remove a gravitational signal of all known density structures and density interfaces within the lithosphere (that includes the crust and the uppermost mantle). In addition, a gravitational signature of the lithosphere-asthenosphere boundary has to be treated according to an adopted density contrast model at this interface. Spectral expressions used for a gravimetric forward modelling of the lithospheric density structure are summarized next.

2.1. Gravity field

For the external convergence domain $r \geq \mathrm{R}$, the disturbing potential T (i.e., the difference between the actual and normal gravity potential W and U respectively; $T = W - U$) at a location (r, Ω) is computed from the disturbing potential coefficients $T_{n,m}$ as follows [17].

$$T(r,\Omega) = \frac{\mathrm{GM}}{\mathrm{R}} \sum_{n=0}^{\bar{n}} \sum_{m=-n}^{n} \left(\frac{\mathrm{R}}{r}\right)^{n+1} T_{n,m} Y_{n,m}(\Omega), \tag{1}$$

where $\mathrm{GM} = 3986005 \times 10^8 \mathrm{m}^3\ \mathrm{s}^{-2}$ is the geocentric gravitational constant, $\mathrm{R} = 6371 \times 10^3$ m is the Earth's mean radius, $Y_{n,m}$ are the surface spherical functions of degree n and order m, and $\bar{n}$ is the upper summation index of spherical harmonics. The disturbing potential coefficients $T_{n,m}$ are obtained from the coefficients of the Earth's gravitational model after subtracting the coefficients describing the GRS80 normal gravity field [18]. The 3-D position in Eq. (1) and thereafter is defined in the spherical coordinate system (r, Ω); where r is the radius, and $\Omega = (\phi, \lambda)$ is the spherical direction with the spherical latitude ϕ and longitude λ. Note that spectral expressions for computing gravity field quantities, such as the gravity disturbances or gravity gradients, could readily be derived from Eq. (1).

2.2. Topographic and crustal corrections

In the most generalized case, corrections to gravity field quantities due to known density structures can be computed based on a method developed by Tenzer et al. [19], which utilizes the information about a 3-D density distribution within particular geological unit, such as sedimentary basins (see also [20–22]). The generic expression for a spherical harmonic synthesis of the gravitational potential reads

$$V(r,\Omega) = \frac{\mathrm{GM}}{\mathrm{R}} \sum_{n=0}^{\bar{n}} \sum_{m=-n}^{n} \left(\frac{\mathrm{R}}{r}\right)^{n+1} V_{n,m} Y_{n,m}(\Omega). \tag{2}$$

By analogy with the computation of gravity field quantities, the expressions for computing corrections to these gravity field quantities, such as the topographic gravity or gravity gradient corrections, could be derived from Eq. (2)

The potential coefficients $V_{n,m}$ of each volumetric mass density layer are defined by

$$V_{n,m} = \frac{3}{2n+1} \frac{1}{\bar{\rho}^{\mathrm{Earth}}} \sum_{i=0}^{I} \left(Cl_{n,m}^{(i)} - Cu_{n,m}^{(i)}\right), \tag{3}$$

where $\bar{\rho}^{\mathrm{Earth}} = 5500\ \mathrm{kgm}^{-3}$ is the Earth's mean mass density, and the coefficients $Cl_{n,m}^{(i)}$ and $Cu_{n,m}^{(i)}$ are given by

$$Cl_{n,m}^{(i)} = \sum_{k=0}^{n+2} \binom{n+2}{k} \frac{(-1)^k}{k+1+i} \frac{C_{L_{n,m}}^{(k+1+i)}}{\mathrm{R}^{k+1}},\quad Cu_{n,m}^{(i)} = \sum_{k=0}^{n+2} \binom{n+2}{k} \frac{(-1)^k}{k+1+i} \frac{C_{U_{n,m}}^{(k+1+i)}}{\mathrm{R}^{k+1}}. \tag{4}$$

The coefficients $C_{L_{n,m}}^{(k+1+i)}$ and $C_{U_{n,m}}^{(k+1+i)}$ in Eq. (4) describe the geometry and density (or density contrast) distribution within a particular crustal density layer (down to the Moho density interface). These coefficients are generated from discrete data (of depth, thickness, and density) using the following expressions for a spherical harmonic analysis [4].

$$C_{L_n}^{(k+1+i)} = \begin{cases} \dfrac{2n+1}{4\pi}\iint_{\Phi}\rho(C_U,\Omega')C_L^{k+1}(\Omega')P_n(t)d\Omega' \\ = \sum_{m=-n}^{n} C_{L_{n,m}}^{(k+1)}Y_{n,m}(\Omega) \qquad i=0 \\ \dfrac{2n+1}{4\pi}\iint_{\Phi}\beta(\Omega')\alpha_i(\Omega')C_L^{k+1+i}(\Omega')P_n(t)d\Omega' \\ = \sum_{m=-n}^{n} C_{L_{n,m}}^{(k+1+i)}Y_{n,m}(\Omega) \qquad i=1,2,\ldots,I \end{cases} \tag{5}$$

and

$$C_{U_n}^{(k+1+i)}(\Omega) = \begin{cases} \dfrac{2n+1}{4\pi}\iint_{\Phi}\rho(C_U,\Omega')C_U^{k+1}(\Omega')P_n(t)d\Omega' \\ = \sum_{m=-n}^{n} C_{U_{n,m}}^{(k+1)}Y_{n,m}(\Omega) \qquad i=0 \\ \dfrac{2n+1}{4\pi}\iint_{\Phi}\beta(\Omega')\alpha_i(\Omega')C_U^{k+1+i}(\Omega')P_n(t)d\Omega' \\ = \sum_{m=-n}^{n} C_{U_{n,m}}^{(k+1+i)}Y_{n,m}(\Omega) \qquad i=1,2,\ldots,I \end{cases} \tag{6}$$

where P_n is the Legendre polynomial for the argument t of cosine of the spherical angle ψ between two points (r,Ω) and (r',Ω'), i.e. $t = \cos\psi$. The infinitesimal surface element on the unit sphere is denoted as $d\Omega' = \cos\phi' d\phi' d\lambda'$, and Φ is the full spatial angle. The geometry of each crustal layer is defined by depths C_U and C_L of the upper and lower bound respectively.

The integral convolutions in Eqs. (5) and (6) utilize a 3-D density distribution ρ defined by the following regression function

$$\rho(r,\Omega) = \rho(C_U,\Omega) + \beta(\Omega)\sum_{i=1}^{I}\alpha_i(\Omega)(\mathrm{R}-r)^i \qquad for \quad \mathrm{R}-C_U(\Omega) \geq r > \mathrm{R}-C_L(\Omega), \tag{7}$$

where $\rho(C_U,\Omega)$ is a (nominal) value of lateral density at a location Ω and depth C_U, and the coefficients α_i and β describe a radial density distribution for each lateral column.

The 3-D density contrast model with respect to the reference lithospheric density ρ^{lith} is defined as

$$\delta\rho(r,\Omega') = \rho(r,\Omega) - \rho^{\mathrm{lith}}, \tag{8}$$

with $\rho(r,\Omega)$ given in Eq. (7).

Note that various density values ρ^{lith} could be adopted to represent the reference density of a particular layer within the lithosphere. In this respect, a reference topographic density typically differs from a reference density that represents the remaining lithosphere below sea level. A more detailed discussion is given next.

2.3. Bouguer gravity field

The corrections (computed according to Eqs. (2)–(8)) are first applied to the disturbing potential T in order to remove the gravitational signal of topography and anomalous density structures within the whole crust. In principle, this procedure is realized by applying the topographic correction V^T in order to remove the gravitational contribution of a uniform topographic density. The density of upper continental crust of 2670 kgm^{-3} [23] is typically adopted to represent a uniform topographic density. Subsequently, additional corrections are applied in order to remove the gravitational contribution due to crust density heterogeneities, where these corrections are computed individually for density contrasts of the bathymetry V^B [24–26], ice V^I [27], sediments V^S [28], and consolidated crust V^C. For density heterogeneities within the topography (i.e. above sea level) the ice, sediment and consolidated crust corrections are computed with respect to an adopted value of the reference topographic density, while for crust density heterogeneities distributed below sea level the density contrast is defined with respect to the reference lithospheric density ρ^{lith} (Eq. (8)). The density value of 2900 kgm^{-3} could be adopted [29]. Noteworthy, the atmospheric correction to the disturbing potential is completely negligible [30]. The computation of the Bouguer potential T^{cs} is then realized according to the following scheme [19].

$$T^{cs} = T - V^T - V^B - V^I - V^S - V^C. \tag{9}$$

Tenzer et al. [31] demonstrated that the Bouguer potential field has a prevailing long-wavelength pattern with maxima distributed in central Pacific and minima in central Eurasia. The Bouguer gravity disturbances are, on the other hand, spatially highly correlated with a Moho geometry [32], and a spatial pattern of the corresponding vertical gravity gradient reflects mainly the largest horizontal spatial variations of the Bouguer gravity disturbances along continental margins and along foothills of Himalaya [33].

2.4. Mantle lithosphere correction

In addition to corrections applied in section 2.3, the gravitational contribution of mantle lithosphere density heterogeneities V^{UM} has to be removed from the Bouguer gravity field T^{cs}. We then write

$$T^A = T^{cs} - V^{UM}. \tag{10}$$

If we assume a lateral density model (according to, for instance, the CRUST1.0 global seismic crustal model that includes also the uppermost mantle density distribution [34]) within the mantle lithosphere, the corresponding gravitational contribution V^{UM} can be computed using the following expression

$$V^{UM}(r,\Omega) = 3\frac{\mathrm{GM}}{\mathrm{R}\bar{\rho}^{\mathrm{Earth}}}\sum_{n=0}^{\bar{n}}\frac{1}{2n+1}\left(\frac{\mathrm{R}}{r}\right)^{n+1} \times \sum_{k=0}^{n+2}\binom{n+2}{k}\frac{(-1)^k}{\mathrm{R}^{k+1}(k+1)}\sum_{m=-n}^{n}\left(L_{n,m}^{(k+1)} - \mathrm{M}_{n,m}^{(k+1)}\right)Y_{n,m}(\Omega). \tag{11}$$

The Moho coefficients $M_{n,m}^{(k+1)}$ in Eq. (11) are introduced in the following form

$$\sum_{m=-n}^{n} \mathrm{M}_{n,m}^{(k)} \mathrm{Y}_{n,m}(\Omega) = \frac{2n+1}{4\pi} \iint_{\Phi} \delta\rho^{UM}(\Omega') M^{k}(\Omega') P_n(t) d\Omega', \tag{12}$$

where $\delta\rho^{UM}(\Omega') = \rho^{UM}(\Omega') - \rho^{\mathrm{lith}}$ is the lateral density contrast of mantle lithosphere ρ^{UM} with respect to the reference lithospheric density ρ^{lith}, and M is the Moho depth. The Moho under oceans is typically 10–15 km deep. The average Moho depth under continents is about 30–35 km and reaches maxima of about 70–80 km under orogens of Andes, Himalaya, and Tibet.

Similarly, we define the lithosphere coefficients $L_{n,m}^{(k+1)}$ in Eq. (11) as follows

$$\sum_{m=-n}^{n} \mathrm{L}_{n,m}^{(k)} \mathrm{Y}_{n,m}(\Omega) = \frac{2n+1}{4\pi} \iint_{\Phi} \delta\rho^{UM}(\Omega') L^{k}(\Omega') P_n(t) d\Omega', \tag{13}$$

where L is depth of the lithosphere-asthenosphere boundary. It is worth mentioning that a thickness of the oceanic lithosphere is typically between 50 and 140 km, while the continental lithosphere is mostly within 100–250 km thick [35], except for some oldest cratonic formations.

If we take into consideration that currently available global lithospheric density models have a 1×1 arc-deg spatial resolution that corresponds (by means of a half wavelength) to a spectral resolution up to the degree of 180, the computation of V^{UM} according to Eq. (11) can be realized using a binomial series up to the third-order term, so that

$$\begin{aligned} V^{UM}(r,\Omega) \cong\, & 3\frac{\mathrm{GM}}{\mathrm{R}^2\bar{\rho}^{\mathrm{Earth}}} \sum_{n=0}^{\bar{n}} \frac{1}{2n+1} \left(\frac{\mathrm{R}}{r}\right)^{n+1} \sum_{m=-n}^{n} \left(L_{n,m} - M_{n,m}\right) Y_{n,m}(\Omega) \\ & - \frac{3}{2}\frac{\mathrm{GM}}{\mathrm{R}^3\bar{\rho}^{\mathrm{Earth}}} \sum_{n=0}^{\bar{n}} \frac{n+2}{2n+1} \left(\frac{\mathrm{R}}{r}\right)^{n+1} \sum_{m=-n}^{n} \left(L_{n,m}^{(2)} - M_{n,m}^{(2)}\right) Y_{n,m}(\Omega) \\ & + \frac{1}{2}\frac{\mathrm{GM}}{\mathrm{R}^4\bar{\rho}^{\mathrm{Earth}}} \sum_{n=0}^{\bar{n}} \frac{(n+2)(n+1)}{2n+1} \left(\frac{\mathrm{R}}{r}\right)^{n+1} \sum_{m=-n}^{n} \left(L_{n,m}^{(3)} - M_{n,m}^{(3)}\right) Y_{n,m}(\Omega). \end{aligned} \tag{14}$$

We note here that a density of the oceanic lithosphere is mainly controlled by conductive cooling. This density distribution is thus characterized by minima along oceanic spreading ridges, increasing density with age of the oceanic lithosphere, and maxima along oceanic subductions [36]. Compared to a relatively homogenous density of the oceanic lithosphere, the continental lithosphere is characterized by much more complex density structure.

2.5. Mantle gravity field

When disregarding errors due to uncertainties of a lithospheric density model, values of T^{A} should theoretically comprise mainly a gravitational signature of the lithosphere-asthenosphere geometry that is superimposed over a weaker signal of the asthenosphere, the transition zone, and the lower mantle including the (Gutenberg) core-mantle boundary zone (D"). To detect this gravitational signal, a gravitational signature of the lithosphere-asthenosphere boundary should be modelled and subsequently removed. This numerical procedure is realized by subtracting the gravitational contribution of a volumetric mass density contrast layer that geometrically involves the lithosphere without the topography and of which density contrast is defined as a difference between the asthenospheric and (reference) lithospheric density [37,38]. Denoting the gravitational contribution of this layer as V^{SL}, we write

$$T^{SM} = T^{A} - V^{SL}, \tag{15}$$

It is important to emphasize that the actual lithosphere-asthenosphere boundary (LAB) is rheological. Studies suggest the existence of compositional or chemical density contrast of 0–20 $\mathrm{kg \cdot m^{-3}}$ [39], except probably the cratonic mantle. In addition to a possibly chemical density contrast, strong thermal density contrast of 30–60 $\mathrm{kg \cdot m^{-3}}$ occurs when the asthenosphere is locally uplifted by rifting.

The computation of V^{SL} is done using the following expression

$$\begin{aligned} V^{SL}(r,\Omega) = & 3\frac{\mathrm{GM}}{\mathrm{R}\bar{\rho}^{\mathrm{Earth}}} \sum_{n=0}^{\bar{n}} \frac{1}{2n+1} \left(\frac{\mathrm{R}}{r}\right)^{n+1} \\ & \times \sum_{k=0}^{n+2} \binom{n+2}{k} \frac{(-1)^k}{\mathrm{R}^{k+1}(k+1)} \sum_{m=-n}^{n} \widehat{L}_{n,m}^{(k+1)} Y_{n,m}(\Omega). \end{aligned} \tag{16}$$

The coefficients $\widehat{L}_{n,m}^{(k+1)}$ in Eq. (16) are defined by

$$\sum_{m=-n}^{n} \widehat{L}_{n,m}^{(k)} Y_{n,m}(\Omega) = \frac{2n+1}{4\pi} \iint_{\Phi} \Delta\rho^{\mathrm{L/A}} L^{k}(\Omega') P_n(t) d\Omega', \tag{17}$$

where L is depth of the lithosphere-asthenosphere boundary (see also Eq. (13)), and $\Delta\rho^{\mathrm{L/A}}$ is the lithosphere-asthenosphere density contrast. We note here that the computation of V^{SL} can again be restricted up to the third-order terms of binomial series.

As stated above, the numerical step of removing a gravitational signal of the lithosphere-asthenosphere boundary should optimally reveal a gravitational signature of deeper mantle density heterogeneities. The resulting gravity field T^{SM} should theoretically be the most suitable for a modelling and interpretations of the mantle density structure (below the lithosphere).

3. Mantle density model

In order to formulate a functional relation between the gravitational field T^{SM} and the corresponding mantle density structure below the lithosphere, a theoretical density distribution model has to be predefined.

Let us assume that the mantle below the lithosphere is separated into several individual volumetric mass density layers. Note again that the density structure within the lithosphere is already taken into consideration. In this way, we could allocate the first volumetric mass layer to represent the asthenosphere. To adopt a unified notation, the upper bound of this layer, defined by the lithosphere-asthenosphere boundary with a variable depth, is denoted as U_1. In the simplest case, the lower bound of this layer is a spherically symmetric, having a constant depth $U_2 = const$ of 410 km. The asthenosphere layer is represented by a 3-D density distribution model with a radial density change described by a regression function up to the second-order term, so that

$$\begin{aligned} \rho(r,\Omega) = \rho(U_1,\Omega) + \beta \sum_{i=1}^{2} \alpha_i (\mathrm{R} - r)^i \\ for \quad \mathrm{R} - U_1(\Omega) \geq r > \mathrm{R} - U_2. \end{aligned} \tag{18}$$

The second layer could represent the mantle transition zone, with the lower bound having again a constant depth $U_3 = const$ of 660 km [40]. We can then apply one or more spherically symmetric layers to represent the lower mantle down to the core-mantle

boundary zone that could be represented by an additional layer. The layer for the core-mantle boundary zone can be considered between depths of 2700 and 2900 km, thus again assuming a constant depth, despite it is believed that the core-mantle boundary has an irregular geometry with variations of about 50 km. The density model is then spherically symmetric, except for the upper bound of the asthenosphere (i.e. the lithosphere-asthenosphere boundary) with a variable depth that could be retrieved from an available lithospheric thickness model, for instance, complied by Conrad and Lithgow-Bertelloni [35]. By analogy with a 3-D density distribution model for the asthenosphere in Eq. (18), the same density description can be adopted for the transition zone, the lower mantle and the core-mantle boundary zone, but for each layer using different density parameters.

According to a theoretical density model proposed above, the surface spherical harmonics describing the lithosphere-asthenosphere boundary are given by

$$ {}_1U_n(\Omega)=\frac{2n+1}{4\pi}\iint_{\Phi}\left[{}_1\rho\left({}_1U,\Omega'\right){}_1U(\Omega')+{}_1\beta\sum_{i=1}^{2}{}_1\alpha_{i1}U^i(\Omega')\right]P_n(t)d\Omega', \tag{19} $$

where ${}_1U=L$ is depth of the lithosphere-asthenosphere boundary.

The corresponding surface spherical harmonics of a lower bound of the asthenosphere are defined by

$$ {}_2U_n(\Omega)=\frac{2n+1}{4\pi}\iint_{\Phi}\left[{}_1\rho\left({}_1U,\Omega'\right){}_2U+{}_1\beta\sum_{i=1}^{2}{}_1\alpha_{i2}U^i\right]P_n(t)d\Omega', \tag{20} $$

where ${}_2U=const$.

For a remaining part of the mantle, we then write

$$ {}_qU_n(\Omega)=\frac{2n+1}{4\pi}\iint_{\Phi}\left[{}_q\rho({}_qU,\Omega'){}_qU+{}_q\beta\sum_{i=1}^{2}{}_q\alpha_{iq}U^i\right]P_n(t)d\Omega' \tag{21} $$

$(q=3, 4, \ldots, Q)$.

From Eqs. (19) and (20), we get

$$ {}_2U_n(\Omega)-{}_1U_n(\Omega)=\frac{2n+1}{4\pi}\iint_{\Phi}{}_1\rho\left({}_1U,\Omega'\right)\left[{}_2U-{}_1U(\Omega')\right]P_n(t)d\Omega' $$

$$ +\frac{2n+1}{4\pi}\iint_{\Phi}{}_1\beta\sum_{i=1}^{2}{}_1\alpha_i\left[{}_2U^i-{}_1U^i(\Omega')\right]P_n(t)d\Omega'. \tag{22} $$

A density model of remaining mantle structure is then described by

$$ \sum_{q=1}^{Q-2}{}_{q+2}U_n(\Omega)-{}_{q+1}U_n(\Omega)=\frac{2n+1}{4\pi}\iint_{\Phi}{}_{q+1}\rho\left({}_{q+1}U,\Omega'\right)\left[{}_{q+2}U-{}_{q+1}U\right]P_n(t)d\Omega' $$

$$ +\frac{2n+1}{4\pi}\iint_{\Phi}{}_{q+1}\beta\sum_{i=1}^{2}{}_{q+1}a_i\left[{}_{q+2}U^i-{}_{q+1}U^i\right]P_n(t)d\Omega' \tag{23} $$

where $\{{}_qU:\ q=1,\ 2,\ \ldots,\ Q\}$, and $Q-1$ is a total number of layers.

3.1. Linearization

To find corrections to a priori density model, we apply a linearization. For the lithosphere-asthenosphere boundary we get

$$ {}_1U_{0_n}(\Omega)+\left.\frac{\partial_1U_n}{\partial_1\rho}\right|_{{}_1\rho_0}d\rho\left({}_1U,\Omega'\right)+\left.\frac{\partial_1U_n}{\partial_1\beta}\right|_{{}_1\beta_0}{}_1d\beta+\sum_{i=1}^{2}{}_1\alpha_i\left.\frac{\partial_1U_n}{\partial_1\alpha_i}\right|_{{}_1\alpha_{0_i}}{}_1d\alpha_i $$

$$ =\frac{2n+1}{4\pi}\iint_{\Phi}\left[{}_1\rho_0\left({}_1U,\Omega'\right){}_1U(\Omega')+{}_1\beta_0\sum_{i=1}^{2}{}_1\alpha_{0_i}{}_1U^i(\Omega')\right]P_n(t)d\Omega' $$

$$ +\frac{2n+1}{4\pi}\iint_{\Phi}{}_1d\rho\left({}_1U,\Omega'\right){}_1U(\Omega')P_n(t)d\Omega' $$

$$ +\frac{2n+1}{4\pi}\iint_{\Phi}{}_1d\beta\sum_{i=1}^{2}{}_1\alpha_{0_i}{}_1U^i(\Omega')P_n(t)d\Omega' $$

$$ +\frac{2n+1}{4\pi}\iint_{\Phi}{}_1\beta_0\sum_{i=1}^{2}{}_1d\alpha_{i1}U^i(\Omega')P_n(t)d\Omega', \tag{24} $$

where ${}_1d\rho$, ${}_1d\beta$, and $\{{}_1d\alpha_i:\ i=1,\ 2\}$ are, respectively, the corrections to density parameters ${}_1\rho$, ${}_1\beta$, and $\{{}_1\alpha_i:\ i=1,\ 2\}$. The values of density parameters ${}_1\rho_0$, ${}_1\beta_0$, and $\{{}_1\alpha_{0_i}:\ i=1,\ 2\}$ can be chosen according to an available density model.

By analogy with Eq. (24), we can write a linearized model for remaining spherically-symmetric boundaries of individual volumetric density layers as follows

$$ {}_qU_{0_n}(\Omega)+\left.\frac{\partial_qU_n}{\partial_q\rho}\right|_{{}_q\rho_0}{}_qd\rho({}_qU,\Omega')+\left.\frac{\partial_qU_n}{\partial_q\beta}\right|_{{}_q\beta_0}{}_qd\beta+\sum_{i=1}^{2}{}_q\alpha_i\left.\frac{\partial_qU_n}{\partial_q\alpha_i}\right|_{{}_q\alpha_{0_i}}{}_qd\alpha_i $$

$$ =\frac{2n+1}{4\pi}\iint_{\Phi}\left[{}_q\rho_0({}_qU,\Omega'){}_qU+{}_q\beta_0\sum_{i=1}^{2}{}_q\alpha_{0_i}{}_qU^i\right]P_n(t)d\Omega' $$

$$ +\frac{2n+1}{4\pi}\iint_{\Phi}{}_qd\rho({}_qU,\Omega'){}_qUP_n(t)d\Omega' $$

$$ +\frac{2n+1}{4\pi}\iint_{\Phi}{}_qd\beta\sum_{i=1}^{2}{}_q\alpha_{0_i}{}_qU^iP_n(t)d\Omega' $$

$$ +\frac{2n+1}{4\pi}\iint_{\Phi}{}_q\beta_0\sum_{i=1}^{2}{}_qd\alpha_{iq}U^iP_n(t)d\Omega'. \tag{25} $$

Since the solution for finding all correction terms ${}_qd\rho$, ${}_qd\beta$, and $\{{}_qd\alpha_i: i=1,\ 2\}$ in Eqs. (24) and (25) is unrealistic, the linearized

density model is further simplified only for finding the lateral-density correction terms ${}_q d\rho$. Hence, we write

$$
\begin{aligned}
&{}_1U_{0_n}(\Omega) + \left.\frac{\partial_1 U_n}{\partial_1 \rho}\right|_{{}_1\rho_0} d\rho\left({}_1U, \Omega'\right) \\
&= \frac{2n+1}{4\pi}\iint_{\Phi}\left[{}_1\rho_0\left({}_1U, \Omega'\right){}_1U(\Omega') + {}_1\beta_0\sum_{i=1}^{2}{}_1\alpha_{0_i}{}_1U^i(\Omega')\right]P_n(t)d\Omega' \\
&+\frac{2n+1}{4\pi}\iint_{\Phi}{}_1d\rho\left({}_1U, \Omega'\right){}_1U(\Omega')P_n(t)d\Omega',
\end{aligned}
\tag{26}
$$

and

$$
\begin{aligned}
&{}_qU_{0_n}(\Omega) + \left.\frac{\partial_q U_n}{\partial_q \rho}\right|_{{}_q\rho_0} {}_q d\rho({}_qU, \Omega') \\
&= \frac{2n+1}{4\pi}\iint_{\Phi}\left[{}_q\rho_0({}_qU, \Omega'){}_qU + {}_q\beta_0\sum_{i=1}^{2}{}_q\alpha_{0_i}{}_qU^i\right]P_n(t)d\Omega' \\
&+\frac{2n+1}{4\pi}\iint_{\Phi}{}_q d\rho({}_qU, \Omega'){}_qUP_n(t)d\Omega'.
\end{aligned}
\tag{27}
$$

Furthermore, if we assume only a priori depth-density model (for instance PREM) below the asthenosphere without lateral density variations, the expression in Eq. (27) is further simplified to

$$
\begin{aligned}
&{}_qU_{0_n}(\Omega) + \left.\frac{\partial_q U_n}{\partial_q \rho}\right|_{{}_q\rho_0} {}_q d\rho({}_qU, \Omega') \\
&= \frac{2n+1}{4\pi}\iint_{\Phi}\left[{}_q\rho_0({}_qU){}_qU + {}_q\beta_0\sum_{i=1}^{2}{}_q\alpha_{0_i}{}_qU^i\right]P_n(t)d\Omega' \\
&+\frac{2n+1}{4\pi}\iint_{\Phi}{}_q d\rho({}_qU, \Omega'){}_qUP_n(t)d\Omega'.
\end{aligned}
\tag{28}
$$

A linearized density model is then described by

$$
\begin{aligned}
&\left[{}_2U_{0_n}(\Omega) - {}_1U_{0_n}(\Omega)\right] + \left[\left.\frac{\partial_2 U_n}{\partial_1\rho\left({}_1U\right)}\right|_{{}_1\rho_0} - \left.\frac{\partial_1 U_n}{\partial_1\rho\left({}_1U\right)}\right|_{{}_1\rho_0}\right]{}_1d\rho\left({}_1U, \Omega'\right) \\
&+\sum_{q=2}^{Q-1}\left[{}_{q+1}U_{0_n}(\Omega) - {}_qU_{0_n}(\Omega)\right] + \sum_{q=2}^{Q-1}\left[\left.\frac{\partial_{q+1}U_n}{\partial_q\rho\left({}_{q+1}U\right)}\right|_{{}_q\rho_0} - \left.\frac{\partial_q U_n}{\partial_q\rho\left({}_qU\right)}\right|_{{}_q\rho_0}\right]{}_q d\rho({}_qU, \Omega') \\
&= \frac{2n+1}{4\pi}\iint_{\Phi}\left\{{}_1\rho_0\left({}_1U, \Omega'\right)\left[{}_2U - {}_1U(\Omega')\right] + {}_1\beta_0\sum_{i=2}^{2}{}_1\alpha_{0_i}\left[{}_2U - {}_1U(\Omega')\right]\right\}P_n(t)d\Omega' \\
&+\frac{2n+1}{4\pi}\iint_{\Phi}\sum_{q=2}^{Q-1}\left[{}_q\rho_0({}_qU)\left({}_{q+1}U - {}_qU\right) + {}_q\beta_0\sum_{i=2}^{2}{}_q\alpha_{0_i}\left({}_{q+1}U^i - {}_qU^i\right)\right]P_n(t)d\Omega' \\
&+\frac{2n+1}{4\pi}\iint_{\Phi}{}_1d\rho\left({}_1U, \Omega'\right)\left[{}_2U - {}_1U(\Omega')\right]P_n(t)d\Omega' \\
&+\frac{2n+1}{4\pi}\iint_{\Phi}\sum_{q=2}^{Q-1}{}_q d\rho({}_qU, \Omega')\left({}_{q+1}U - {}_qU\right)P_n(t)d\Omega'.
\end{aligned}
\tag{29}
$$

As seen in Eq. (29), a linearized mantle density model (below the lithosphere) is defined for the asthenosphere with a variable depth of the upper bound (i.e. the lithosphere-asthenosphere boundary), while a spherically-symmetric volumetric layers describes mantle density structure below the asthenosphere. Each layer is described individually by parameters β and $\{\alpha_i : \ i = 1, 2\}$ of a priori depth-density model, while lateral density variations are unknown parameters. It is worth mentioning that the assumption of different depth-density parameters for each volumetric mass layer is relevant when proposing a mantle density model complied using seismic data. On the other hand, PREM describes the change of density with depth within the mantle below the lithosphere using the same (second-order) depth-dependent parameters (see Fig. 1).

4. Functional relation between mass density and gravity field

A linearized model in Eq. (29) describes a density distribution based on adopting a priori parameters that define a radial density distribution, while lateral density changes within each volumetric mass layer have to be computed using, for instance, seismic data. A forward modelling technique can then be applied to compute the gravitational field of this mantle density model (below the lithosphere). The gravitational contribution of the core should theoretically be zero after removing the normal gravity field for optimally chosen spherically symmetric density reference field. This gravitational contribution can then be compared with the gravitational field T^{SM} that was obtained from observed gravity field after subtracting the gravitational contribution of lithospheric density heterogeneities and a subsequent adding the gravitational contribution of a reference lithosphere. To combine these two solutions that describes a gravitational contribution of the mantle below the lithosphere, we derive a functional model that links density and gravity models.

4.1. Linearized functional model

To link a density model (given in Eq. (29)) with the gravity field T^{SM} (computed according to Eqs. (1)–(15)), we first write

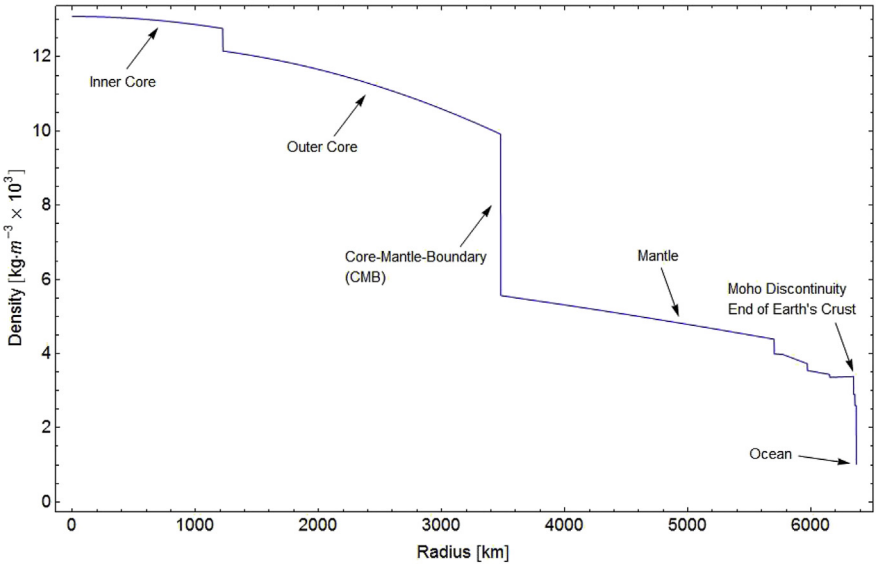

Fig. 1. Earth's depth-density distribution according to the Preliminary Reference Earth Model - PREM [11].

$$T^{SM}(r,\Omega)=\frac{GM}{R}\sum_{n=0}^{\bar{n}}\left(\frac{R}{r}\right)^{n+1}\sum_{m=-n}^{n}\sum_{q=1}^{Q-1}{}_qV^{SM}_{n,m}Y_{n,m}(\Omega)+V^L(r,\Omega)+\varepsilon_{V^L}(r,\Omega), \tag{30}$$

where $\{{}_qV^{SM}_{n,m}: q=1,\ 2,\ldots,Q-1\}$ are the potential coefficients describing the gravitational contribution of volumetric mass density layers within the mantle below the lithosphere, and V^L is the gravitational contribution of a reference lithosphere (without the topographic mases) of which density is taken with respect to the upper asthenosphere density model (section 2.5), and ε_{V^L} denotes errors that are mainly attributed to density uncertainties of used lithospheric model.

We further define the potential coefficients $V^{SM}_{n,m}$ in Eq. (30) as follows

$${}_qV^{SM}_{n,m}=\frac{3}{2n+1}\frac{1}{\bar{\rho}^{\mathrm{Earth}}}\sum_{i=0}^{2}\left({}_qFl^{(i)}_{n,m}-{}_qFu^{(i)}_{n,m}\right), \tag{31}$$

where the coefficients ${}_qFl^{(i)}_{n,m}$ and ${}_qFu^{(i)}_{n,m}$ are introduced by

$$\begin{aligned}{}_qFl^{(i)}_{n,m}&=\sum_{k=0}^{n+2}\binom{n+2}{k}\frac{(-1)^k}{k+1+i}\frac{{}_qF^{(k+1+i)}_{L_{n,m}}}{R^{k+1}}\\ {}_qFu^{(i)}_{n,m}&=\sum_{k=0}^{n+2}\binom{n+2}{k}\frac{(-1)^k}{k+1+i}\frac{{}_qF^{(k+1+i)}_{U_{n,m}}}{R^{k+1}}\end{aligned} \tag{32}$$

From Eq. (19), we can define the coefficients ${}_1F^{(k+1+i)}_{U_{n,m}}$ (i.e. for $q=1$) individually for the lithosphere-asthenosphere boundary (of a variable depth) as follows

$${}_1F^{(k+1+i)}_{U_n}(\Omega)=\begin{cases}\dfrac{2n+1}{4\pi}\displaystyle\iint_{\Phi}{}_1\rho\left({}_1U,\Omega'\right){}_1U^{k+1}(\Omega')P_n(t)d\Omega'\\ =\displaystyle\sum_{m=-n}^{n}{}_1F^{(k+1)}_{U_{n,m}}Y_{n,m}(\Omega)\qquad i=0\\ \dfrac{2n+1}{4\pi}\displaystyle\iint_{\Phi}{}_1\beta_1\alpha_{i1}U^{k+1+i}(\Omega')P_n(t)d\Omega'\\ =\displaystyle\sum_{m=-n}^{n}{}_1F^{(k+1+i)}_{U_{n,m}}Y_{n,m}(\Omega)\qquad i=1,\ 2\end{cases} \tag{33}$$

The corresponding coefficients ${}_1F^{(k+1+i)}_{Ln,m}$ of a lower bound of the asthenosphere then read

$${}_1F^{(k+1+i)}_{Ln}(\Omega)=\begin{cases}\dfrac{2n+1}{4\pi}\displaystyle\iint_{\Phi}{}_1\rho\left({}_1U,\Omega'\right){}_2U^{k+1}P_n(t)d\Omega'\\ =\displaystyle\sum_{m=-n}^{n}{}_qF^{(k+1)}_{L_{n,m}}Y_{n,m}(\Omega)\qquad i=0\\ \dfrac{2n+1}{4\pi}\displaystyle\iint_{\Phi}{}_1\beta_1\alpha_{i2}U^{k+1+i}P_n(t)d\Omega'\\ =\displaystyle\sum_{m=-n}^{n}{}_1F^{(k+1+i)}_{L_{n,m}}Y_{n,m}(\Omega)\qquad i=1,\ 2\end{cases} \tag{34}$$

Similarly, the coefficients $\{{}_qF^{(k+1+i)}_{L_{n,m}},\ {}_qF^{(k+1+i)}_{U_{n,m}},\ q=2,\ 3,\ldots,\ Q-1\}$ of spherically-symmetric layers are given by

$$ {}_qF_{L_n}^{(k+1+i)}(\Omega)=\begin{cases}\dfrac{2n+1}{4\pi}\iint_{\Phi}{}_q\rho\left({}_qU\right){}_{q+1}U^{k+1}P_n(t)d\Omega' & \\ =\sum\limits_{m=-n}^{n}{}_qF_{L_{n,m}}^{(k+1)}Y_{n,m}(\Omega) & i=0\\ \dfrac{2n+1}{4\pi}\iint_{\Phi}{}_q\beta_q\alpha_{iq+1}U^{k+1+i}P_n(t)d\Omega' & \\ =\sum\limits_{m=-n}^{n}{}_qF_{L_{n,m}}^{(k+1+i)}Y_{n,m}(\Omega) & i=1,\ 2\end{cases} \tag{35}$$

and

$$ {}_qF_{U_n}^{(k+1+i)}(\Omega)=\begin{cases}\dfrac{2n+1}{4\pi}\iint_{\Phi}{}_q\rho\left({}_qU\right){}_qU^{k+1}P_n(t)d\Omega' & \\ =\sum\limits_{m=-n}^{n}{}_qF_{U_{n,m}}^{(k+1)}Y_{n,m}(\Omega) & i=0\\ \dfrac{2n+1}{4\pi}\iint_{\Phi}{}_q\beta_q\alpha_{iq}U^{k+1+i}P_n(t)d\Omega' & \\ =\sum\limits_{m=-n}^{n}{}_qF_{U_{n,m}}^{(k+1+i)}Y_{n,m}(\Omega) & i=1,\ 2\end{cases} \tag{36}$$

Let us now apply a linearization of coefficients $V_{n,m}^{SM}$ according to the scheme proposed for a mantle density model in Eqs. 26–29. We write

$$ {}_qV_{n,m}^{SM}={}_qV_{0_{n,m}}^{SM}+\left({}_qa_{L_{n,m}}-{}_qa_{U_{n,m}}\right)\Big|_{{}_q\rho_0}{}_qd\rho({}_qU,\Omega'), \tag{37}$$

where

$$ {}_qa_{L_{n,m}}=\frac{\partial_qV_{0_{n,m}}^{SM}}{\partial_qFl_{n,m}^{(i)}}\frac{\partial_qFl_{n,m}^{(i)}}{\partial_qF_{L_{n,m}}^{(k+1+i)}}\frac{\partial_qF_{L_{n,m}}^{(k+1+i)}}{\partial_q\rho\left({}_qU,\Omega'\right)} \tag{38}$$

and

$$ {}_qa_{U_{n,m}}=\frac{\partial_qV_{0_{n,m}}^{SM}}{\partial_qFu_{n,m}^{(i)}}\frac{\partial_qFu_{n,m}^{(i)}}{\partial_qF_{L_{n,m}}^{(k+1+i)}}\frac{\partial_qF_{L_{n,m}}^{(k+1+i)}}{\partial_q\rho\left({}_qU,\Omega'\right)} \tag{39}$$

The coefficients ${}_qV_{0_{n,m}}^{SM}$ are evaluated according to adopted a priori mantle density model (such as PREM) as follows

$$ {}_qV_{0_{n,m}}^{SM}=\frac{3}{2n+1}\frac{1}{\bar{\rho}^{\text{Earth}}}\sum_{i=0}^{2}\sum_{k=0}^{n+2}\binom{n+2}{k}\frac{(-1)^k}{k+1+i}\frac{{}_qF_{L0_{n,m}}^{(k+1+i)}-{}_qF_{U0_{n,m}}^{(k+1+i)}}{\mathrm{R}^{k+1}} \quad (q=1,2,\ldots Q-1) \tag{40}$$

where the coefficients ${}_qF_{L0_{n,m}}^{(k+1+i)}$ and ${}_qF_{U0_{n,m}}^{(k+1+i)}$ are computed according to expressions in Eqs. 33–36 using the nominal density parameters ${}_q\rho_0({}_qU)$, ${}_q\beta_0$, and $\{{}_q\alpha_{0_i}:\ i=1,\ 2\}$.

The terms ${}_qa_{L_{n,m}}$ and ${}_qa_{U_{n,m}}$ in Eqs. (38) and (39) are found to be

$$ {}_qa_{L_{n,m}}=\frac{3}{2n+1}\frac{1}{\bar{\rho}^{\text{Earth}}}\sum_{k=0}^{n+2}\binom{n+2}{k}\frac{(-1)^k}{k+1}\frac{{}_qF_{L0_{n,m}}^{(k+1)}}{\mathrm{R}^{k+1}},$$

$$ {}_qa_{U_{n,m}}=\frac{3}{2n+1}\frac{1}{\bar{\rho}^{\text{Earth}}}\sum_{k=0}^{n+2}\binom{n+2}{k}\frac{(-1)^k}{k+1}\frac{{}_qF_{U0_{n,m}}^{(k+1)}}{\mathrm{R}^{k+1}}\ (q=1,2,\ldots,Q-1). \tag{41}$$

As seen in Eq. (41), the terms ${}_qa_{L_{n,m}}$ and ${}_qa_{U_{n,m}}$ are computed without involving radial density changes. For $q=1$ we then get

$$ \sum_{m=-n}^{n}{}_1F_{U0_{n,m}}^{(k+1)}Y_{n,m}(\Omega)=\frac{2n+1}{4\pi}\iint_{\Phi}{}_1\rho_0\left({}_1U\right){}_1U^{k+1}(\Omega')P_n(t)d\Omega' \tag{42}$$

For $q=2,\ldots,Q$, we write

$$ \sum_{m=-n}^{n}{}_qF_{U0_{n,m}}^{(k+1)}Y_{n,m}(\Omega)=\frac{2n+1}{4\pi}\iint_{\Phi}{}_q\rho_0\left({}_qU\right){}_qU^{k+1}P_n(t)d\Omega' \tag{43}$$

The lower-bound coefficients are defined by

$$ \sum_{m=-n}^{n}{}_qF_{L0_{n,m}}^{(k+1)}Y_{n,m}(\Omega)=\frac{2n+1}{4\pi}\iint_{\Phi}{}_q\rho_0\left({}_qU\right){}_{q+1}U^{k+1}P_n(t)d\Omega' \quad (q=1,2,\ldots Q-1). \tag{44}$$

4.2. Density corrections

A functional relation derived in section 4.1 is further defined in terms of unknown lateral-density corrections. Inserting from Eq. (37) to Eq. (30), we get

$$ T^{SM}(r,\Omega)-V^L(r,\Omega)=\frac{\mathrm{GM}}{\mathrm{R}}\sum_{n=0}^{\bar{n}}\left(\frac{\mathrm{R}}{r}\right)^{n+1}\sum_{m=-n}^{n}\sum_{q=1}^{Q-1}{}_qV_{0_{n,m}}^{SM}Y_{n,m}(\Omega)+\frac{\mathrm{GM}}{\mathrm{R}}\sum_{n=0}^{\bar{n}}\left(\frac{\mathrm{R}}{r}\right)^{n+1}\sum_{m=-n}^{n}\sum_{q=1}^{Q-1}\left({}_qa_{Ln,m}-{}_qa_{Un,m}\right)\Big|_{{}_q\rho_0}Y_{n,m}(\Omega){}_qd\rho({}_qU,\Omega') \tag{45}$$

Denoting

$$ T_0^{SM}(r,\Omega)=\frac{\mathrm{GM}}{\mathrm{R}}\sum_{n=0}^{\bar{n}}\left(\frac{\mathrm{R}}{r}\right)^{n+1}\sum_{m=-n}^{n}\sum_{q=1}^{Q-1}{}_qV_{0_{n,m}}^{SM}Y_{n,m}(\Omega)$$

$$ =3\frac{\mathrm{GM}}{\mathrm{R}\bar{\rho}^{\text{Earth}}}\sum_{n=0}^{\bar{n}}\left(\frac{\mathrm{R}}{r}\right)^{n+1}\frac{1}{2n+1}\sum_{m=-n}^{n}\sum_{q=1}^{Q-1}\sum_{i=0}^{2}\sum_{k=0}^{n+2}\binom{n+2}{k}\frac{(-1)^k}{k+1+i}\times\frac{{}_qF_{L0_{n,m}}^{(k+1+i)}-{}_qF_{U0_{n,m}}^{(k+1+i)}}{\mathrm{R}^{k+1}}Y_{n,m}(\Omega) \tag{46}$$

we arrive at

$$T^{SM}(r,\Omega)-V^{L}(r,\Omega)-T_0^{SM}(r,\Omega)=$$
$$+\frac{GM}{R}\sum_{n=0}^{\bar{n}}\left(\frac{R}{r}\right)^{n+1}\sum_{m=-n}^{n}\sum_{q=1}^{Q-1}\left({}_qa_{L_{n,m}}-{}_qa_{U_{n,m}}\right)\Big|_{{}_q\rho_0}Y_{n,m}(\Omega)\,{}_qd\rho({}_qU,\Omega'). \tag{47}$$

A substitution for ${}_qa_{L_{n,m}}$ and ${}_qa_{U_{n,m}}$ from Eq. (41) to Eq. (47) yields

$$T^{SM}(r,\Omega)-V^{L}(r,\Omega)-T_0^{SM}(r,\Omega)$$
$$=3\frac{GM}{R\bar{\rho}^{Earth}}\sum_{n=0}^{\bar{n}}\left(\frac{R}{r}\right)^{n+1}\frac{1}{2n+1}\sum_{m=-n}^{n}\sum_{q=1}^{Q-1}{}_qd\rho({}_qU,\Omega') \tag{48}$$
$$\times\sum_{k=0}^{n+2}\binom{n+2}{k}\frac{(-1)^k}{k+1}\frac{{}_qF_{L0_{n,m}}^{(k+1)}-{}_qF_{U0_{n,m}}^{(k+1)}}{R^{k+1}}Y_{n,m}(\Omega).$$

We further rearrange the expression in Eq. (48) so that the first layer (i.e. $q=1$) that represents the asthenosphere is treated separately. Then we write

$$T^{SM}(r,\Omega)-V^{L}(r,\Omega)-T_0^{SM}(r,\Omega)$$
$$=3\frac{GM}{R\bar{\rho}^{Earth}}\sum_{n=0}^{\bar{n}}\left(\frac{R}{r}\right)^{n+1}\frac{1}{2n+1}\sum_{m=-n}^{n}{}_1d\rho\left({}_1U,\Omega'\right)$$
$$\times\sum_{k=0}^{n+2}\binom{n+2}{k}\frac{(-1)^k}{k+1}\frac{{}_1F_{L0_{n,m}}^{(k+1)}-{}_1F_{U0_{n,m}}^{(k+1)}}{R^{k+1}}Y_{n,m}(\Omega) \tag{49}$$
$$+3\frac{GM}{R\bar{\rho}^{Earth}}\sum_{n=0}^{\bar{n}}\left(\frac{R}{r}\right)^{n+1}\frac{1}{2n+1}\sum_{m=-n}^{n}\sum_{q=2}^{Q-1}{}_qd\rho({}_qU,\Omega')$$
$$\times\sum_{k=0}^{n+2}\binom{n+2}{k}\frac{(-1)^k}{k+1}\frac{{}_qF_{L0_{n,m}}^{(k+1)}-{}_qF_{U0_{n,m}}^{(k+1)}}{R^{k+1}}Y_{n,m}(\Omega).$$

After inserting for ${}_qF_{L0_{n,m}}^{(k+1+i)}$ and ${}_qF_{U0_{n,m}}^{(k+1+i)}$ from Eqs. 42–44 to Eq. (49), we arrive at

$$T^{SM}(r,\Omega)-V^{L}(r,\Omega)-T_0^{SM}(r,\Omega)$$
$$=\frac{3}{4\pi}\frac{GM}{R\bar{\rho}^{Earth}}\sum_{n=0}^{\bar{n}}\left(\frac{R}{r}\right)^{n+1}\sum_{k=0}^{n+2}\binom{n+2}{k}\frac{(-1)^k}{k+1}\frac{1}{R^{k+1}}$$
$$\times\iint_{\Phi}{}_1\rho_0\left({}_1U\right)\left[{}_2U^{k+1}-{}_1U^{k+1}(\Omega')\right]{}_1d\rho\left({}_1U,\Omega'\right)P_n(t)d\Omega'$$
$$+\frac{3}{4\pi}\frac{GM}{R\bar{\rho}^{Earth}}\sum_{n=0}^{\bar{n}}\left(\frac{R}{r}\right)^{n+1}\sum_{k=0}^{n+2}\binom{n+2}{k}\frac{(-1)^k}{k+1}\frac{1}{R^{k+1}} \tag{50}$$
$$\times\sum_{q=2}^{Q-1}\iint_{\Phi}{}_q\rho_0({}_qU)\left({}_{q+1}U^{k+1}-{}_qU^{k+1}\right){}_qd\rho({}_qU,\Omega')P_n(t)d\Omega'.$$

Introducing the (lateral) density correction terms

$$\sum_{m=-n}^{n}{}_1d\rho_{n,m}^{(k+1)}Y_{n,m}(\Omega)=\frac{2n+1}{4\pi}\iint_{\Phi}{}_1\rho_0\left({}_1U\right)$$
$$\times\left[{}_2U^{k+1}-{}_1U^{k+1}(\Omega')\right]{}_1d\rho\left({}_1U,\Omega'\right)P_n(t)d\Omega', \tag{51}$$

and

$$\sum_{m=-n}^{n}{}_qd\rho_{n,m}^{(k+1)}Y_{n,m}(\Omega)=\frac{2n+1}{4\pi}\iint_{\Phi}{}_q\rho_0({}_qU)\left({}_{q+1}U^{k+1}-{}_qU^{k+1}\right){}_qd\rho({}_qU,\Omega')P_n(t)d\Omega' \tag{52}$$

$(q=2,\ 3,\ldots,\ Q-1)$,

the linearized observation equation becomes

$$T^{SM}(r,\Omega)-V^{L}(r,\Omega)-T_0^{SM}(r,\Omega)$$
$$=\frac{3}{\bar{\rho}^{Earth}}\frac{GM}{R}\sum_{n=0}^{\bar{n}}\left(\frac{R}{r}\right)^{n+1}\frac{1}{2n+1}\sum_{k=0}^{n+2}\binom{n+2}{k}\frac{(-1)^k}{k+1}\frac{1}{R^{k+1}}\sum_{q=1}^{Q-1}\sum_{m=-n}^{n}{}_qd\rho_{n,m}^{(k+1)}Y_{n,m}(\Omega). \tag{53}$$

Methods for a spherical harmonic analysis and synthesis of gravity and density structure models are used to compute terms on the left-hand side of Eq. (53). More specifically, a gravimetric forward modelling of lithospheric density model (such as CRUST1.0 or LITHO1.0) is applied to compute the values of T^{SM} according the expressions given in Eqs. 1–19. The nominal value of T_0^{SM} is computed according to Eq. (46) for the adopted a priori radial-density model (such as PREM). The gravitational contribution of a reference lithosphere V^L is evaluated using the following expression

$$V^L(r,\Omega)=3\frac{GM}{R\bar{\rho}^{Earth}}\sum_{n=0}^{\bar{n}}\frac{1}{2n+1}\left(\frac{R}{r}\right)^{n+1}\times\sum_{k=0}^{n+2}\binom{n+2}{k}\frac{(-1)^k}{R^{k+1}(k+1)}\sum_{m=-n}^{n}\widehat{L}_{n,m}^{(k+1)}Y_{n,m}(\Omega), \tag{54}$$

with the coefficients $\widehat{L}_{n,m}^{(k+1)}$ defined by

$$\sum_{m=-n}^{n}\widehat{L}_{n,m}^{(k)}Y_{n,m}(\Omega)=\frac{2n+1}{4\pi}\iint_{\Phi}\rho^A L^k(\Omega')P_n(t)d\Omega', \tag{55}$$

where L is depth of the lithosphere-asthenosphere boundary (see also Eq. (13)), and ρ^A is the upper asthenosphere density. We note here that the computation of V^{SL} can again be restricted up to the third-order terms of series.

In the most simplistic case, the system of linearized observation equations defined according to Eq. (53) could be solved to find lateral density variations within a single volumetric layer that represents the mantle structure (below the lithosphere) without further stratification. A gravimetric inversion then becomes equivalent to that applied, for instance, to find depth of the Moho interface of sediment bedrock. To evaluate a more complex density model based on applying a gravity inversion, the mantle (below the lithosphere) obviously have to be divided into more than one volumetric mass layer. In this case, however, a direct inversion of gravity field quantities to mass density values based on solving a system of linearized observation equations (Eq. (53)) is not appropriate due to a non-uniqueness of the solution. Moreover, this inversion scheme is ill-posed.

An alternative method to avoid these theoretical limitations is to use seismic data to determine the density correction coefficients $d\rho_{n,m}^{(k+1)}$ on the right-hand side of Eq. (53). This procedure involves a conversion of seismic velocities to mass densities (or in our case density corrections). These density corrections are then used to compute the corresponding gravitational contribution according to the expression on the left-hand side of Eq. (53). This result can be compared with the gravimetric result obtained by solving the right-hand side of Eq. (53). Furthermore, additional techniques could be applied to improve the fit between a direct gravimetric solution and a corresponding solution based of a conversion of seismic velocity to mass density and subsequently a gravimetric forward modelling. These numerical procedures are discussed next.

5. Seismic velocity to mass density conversion

The density corrections $d\rho_{n,m}^{(k+1)}$ on the right-hand side of Eq. (53) could be computed using an available 3-D global tomographic model of the S-wave and P-wave velocities within the mantle. The seismic velocity anomalies could be converted to mass density anomalies by applying a constant velocity-density scaling [41].

$$r=\frac{d\ln\rho}{d\ln V_{S,P}}, \tag{56}$$

where ρ is the density, and $V_{S,P}$ denotes either the S-wave or P-wave velocity. The scaling factor of 0.25 is typically adopted for the S-wave velocities, while 0.5 for the P-wave velocities throughout the mantle. The dependence of seismic velocities on density in the mantle has been investigated in numerous studies. Some authors suggested a nonlinear relation between them [42–44]. Ghosh et al. [41] tested a depth-dependent scaling with scaling reduced by a factor 2 in the uppermost 220 km; preferred scaling used by Čadek and Fleitout [45] and a radial viscosity structure. They acquired that the constant and the depth-dependent scaling factors yield very similar results when applied to reproduce one of the most remarkable geoid features attributed to mantle density heterogeneities, particularly the Indian Ocean Geoid Low. The constant scaling factor thus might be sufficient for an initial density model. In addition, positive density anomalies in the top 300 km below cratons [46] are set to zero in some cases, although they seem to have a minor effect on gravity field. In principle, the mantle density anomalies are primarily attributed to variations in temperature, but substantial chemical heterogeneity is required in the cratonic roots of continents and partially also in the deepest mantle particularly at locations of super-plumes.

A practical method to compute the density correction coefficients $d\rho_{n,m}^{(k+1)}$ from seismic velocity anomalies can be done in a discrete domain by converting values of seismic velocity anomalies to corresponding values of density anomalies $d\rho$ according to Eq. (56) for a particular scaling factor r (either for the S-wave or P-wave velocities). Discrete values of density anomalies $d\rho$ are then used to generate the density correction coefficients $d\rho_{n,m}^{(k+1)}$ for each volumetric mass density layer according to the following integral convolution

$$\sum_{m=-n}^{n}d\rho_{n,m}^{(k+1)}Y_{n,m}=\frac{2n+1}{4\pi}\iint_{\Phi}d\rho^{k+1}(\Omega')P_n(t)d\Omega'. \tag{57}$$

Various global tomographic mantle models should be used to generate the density correction coefficients according to Eqs. (56) and (57). Among exiting models, we could mention TX2008 [47], S40RTS [48], SAW642AN [49], SEMUCB-WM1 [50], GyPSuM [16] SAVANI [51], SMEAN2 (a composite mantle tomography model composed of S40RTS, GyPSuM-S, and SAVANI generated using the approach of Becker and Boschi [52]) or the recent LLNL-G3D-JPS model [53]. The first four models are S wave models, whereas GyPSuM and LLNL have both P and S wave versions. In this way, we get a set of different mantle density models (below the lithosphere) that could be used to compute the corresponding gravitational contribution according to the expression on the right-hand side of Eq. (53). These results then can be compared with the gravimetric result obtained based on solving the left-hand side of Eq. (53). The mantle density model which provides the best fit (by means of the root-mean-square of differences) with the gravimetric result can then be selected as an optimal solution. However, solutions based on solving the left- and right-hand side of Eq. (53) could be systematically biased. In this case, a further calibration of the scaling factor r can be conducted by applying a trial-and-error technique to find the scaling factor, which minimize the bias between the gravimetric result and the corresponding result based on a conversion of seismic velocities to mass densities. We note that a more refined method for finding optimal scaling factors could be done according to Karato and Karki [54] that takes into consideration differential changes of the elastic moduli in a conversion of seismic velocities to mass densities.

The final mantle density model (below lithosphere) together with the global lithospheric density model (such as LITHO1.0) can be combined together to represent the 3-D Earth's density model down to the core mantle boundary zone, while a spherically symmetric density structure (taken, for instance, from PREM) is adopted for the inner and outer core.

5.1. Validation techniques

An independent validation of Earth's density model could also be conducted. For this purpose, various methods are applied. Probably the most commonly used method is based on the geoid modelling [55]. The geoid is calculated with a spectral resolution up to the maximum spherical harmonic degree that is compatible with the global Earth's density model. The predicted geoid anomaly results from a combination of the internal density anomalies and the dynamic topography at the surface and at the core-mantle boundary [56,57]. The resulting geoid is correlated with the observed geoid which is relative to the hydrostatic equilibrium shape and not the reference ellipsoid [58]. Alternatively, such comparison could be done for the free-air gravity disturbances.

Another method that could be used for the validation is based on using the 3-D density anomalies within the mantle and the radial viscosity profile derived, for instance, by Mitrovica and Forte [59] to reproduce the mantle flow. The dynamic surface topography obtained after applying this method can then be compared the crust-corrected surface topography. We could also mention a method based on predicting tectonic plate motions driven by the total density anomalies in terms of the fit to observed horizontal divergence field according to, for instance, the NUVEL-1 geological model of tectonic motions.

6. Concluding remarks

Numerical schemes have been proposed in this study to compile a mantle density model based on combining global gravitational and seismic data. In principle, two numerical techniques are involved, namely the gravimetric forward modelling of known density structures and the conversion of seismic velocities to mass densities. Both these techniques are required to solve the system of observation equations defined in Eq. (53). In global studies, methods for a spherical harmonic analysis and synthesis of gravitational and density structure data are conveniently applied.

The left-hand side of Eq. (53) is solved by applying the gravimetric forward modelling of the lithospheric density structure based on an available model, such as LITHO1.0 or CRUST1.0. The second part of this computation involves again the gravimetric forward modelling to compute the gravitational contribution of a reference lithosphere (excluding the topography) of which density contrast is defined as the density difference of the asthenosphere and the (reference) lithosphere. The third part involves the computation of the gravitational contribution of the a priori mantle density model (below the lithosphere) according to PREM radial density distribution.

The solution of the right-hand side of Eq. (54) consists of the conversion of seismic velocity anomalies to mass density anomalies followed by the gravimetric forward modelling of the corresponding gravitational contribution of anomalous density corrections obtained from seismic information.

Theoretically, solutions obtained by solving the left- and right-hand side of Eq. (53) should be consistent. It is recommended to test available tomographic models and select the model that best fits the result of the gravimetric forward modelling (i.e. the solution of the left-hand side of Eq. (53)). In the presence of systematic bias, additional numerical procedures could be applied, such as an estimation of a scaling factor for the conversion of seismic velocities to mass densities. The 3-D Earth's density model can then be obtained by combining an available lithospheric model together with the mantle density model below the lithosphere complied according to numerical procedures proposed here. These numerical procedures will be tested and applied to compile Earth's global density model in the forthcoming study.

Conflicts of Interest

The authors declare that there is no conflicts of interest.

Appendix A. Supplementary data

Supplementary data to this article can be found online at https://doi.org/10.1016/j.geog.2019.09.003.

References

[1] S.V. Sobolev, A.Y. Babeyko, Modeling of mineralogical composition, density and elastic wave velocities in anhydrous magmatic rocks, Surv. Geophys. 15 (5) (1994) 515–544.
[2] N.I. Christensen, W.D. Mooney, Seismic velocity structure and composition of the continental crust: a global view, J. Geophys. Res. 100 (B7) (1995) 9761–9788.
[3] A.H. Lachenbruch, P. Morgan, Continental extension, magmatism and elevation; formal relations and rules of thumb, Tectonophysics 174 (1990) 39–62.
[4] F. Birch, The velocity of compressional waves in rocks to 10 kilobars. Part 2, J. Geophys. Res. 66 (1961) 2199–2224.
[5] F. Birch, Density and composition of mantle and core, J. Geophys. Res. 69 (20) (1964) 4377–4388.
[6] D.L. Anderson, A seismic equation of state, Geophys J R Astron Soc 13 (1967) 9–30.
[7] D.L. Anderson, A universal thermal equation-of-slate, J. Geodyn. 1 (1984) 185–214.
[8] D.L. Anderson, A seismic equation of state II. Shear properties and thermodynamics of the lower mantle, Earth Planet. Sci. Lett. 45 (1987) 307–323.
[9] D.L. Anderson, J. Bass, Mineralogy and composition of the upper mantle, Geophys. Res. Lett. 11 (1984) 637–640.
[10] L. Knopoff, Density-velocity relations for rocks, Geophys. J. 13 (1967) 1.
[11] A.M. Dziewonski, D.L. Anderson, Preliminary reference Earth model, Phys. Earth Planet. Inter. 25 (4) (1981) 297–356.
[12] H.C.P. Lau, J.X. Mitrovica, J.L. Davis, J. Tromp, H.Y. Yang, D. Al-Attar, Tidal tomography constrains Earth's deep-mantle buoyancy, Nature 551 (7680) (2017) 321–326.
[13] M.J. Hoggard, N.J. White, D. Al-Attar, *Global dynamic topography* observations reveal limited influence of *large-scale mantle* flow, Nat. Geosci. 9 (2016) 456–463.
[14] N.A. Simmons, H. Gurrola, Multiple seismic discontinuities near the base of the transition zone in the Earth's mantle, Nature 405 (2000) 559–562.
[15] J.F. Lawrence, P.M. Shearer, Constraining seismic velocity and density for the mantle transition zone with reflected and transmitted waveforms, Geochem. Geophys. Geosyst. 7 (2006) Q10012.
[16] N.A. Simmons, A.M. Forte, L. Boschi, S.P. Grand, GyPSuM: a joint tomographic model of mantle density and seismic wave speeds, J. Geophys. Res. 115 (2010) B12310.
[17] W.H. Heiskanen, H. Moritz, Physical Geodesy, WH Freeman and Co, San Francisco, 1967.
[18] H. Moritz, Geodetic reference system 1980, J. Geod. 74 (2000) 128162.
[19] R. Tenzer, Vajda P. Hamayun, Global maps of the CRUST2.0 components stripped gravity disturbances, J. Geophys. Res. (solid Earth) 114 (2009) B05408.
[20] R. Tenzer, P. Novák, P. Vajda, V. Gladkikh, Spectral harmonic analysis and synthesis of Earth's crust gravity field, Comput. Geosci. 16 (1) (2012) 193–207.
[21] R. Tenzer, V. Gladkikh, P. Vajda, P. Novák, Spatial and spectral analysis of refined gravity data for modelling the crust-mantle interface and mantle-lithosphere structure, Surv. Geophys. 33 (5) (2012) 817–839.
[22] R. Tenzer, W. Chen, D. Tsoulis, M. Bagherbandi, L.E. Sjöberg, P. Novák, S. Jin, Analysis of the refined CRUST1.0 crustal model and its gravity field, Surv. Geophys. 36 (1) (2015) 139–165.
[23] W.J. Hinze, Bouguer reduction density, why 2.67? Geophysics 68 (5) (2003) 1559.
[24] V. Gladkikh, R. Tenzer, A mathematical model of the global ocean saltwater density distribution, Pure Appl. Geophys. 169 (1–2) (2011) 249–257.
[25] R. Tenzer, P. Novák, V. Gladkikh, On the accuracy of the bathymetry-generated gravitational field quantities for a depth-dependent seawater density distribution, Studia Geophys. Geod. 55 (4) (2011) 609–626.

[26] R. Tenzer, P. Novák, V. Gladkikh, The bathymetric stripping corrections to gravity field quantities for a depth-dependent model of the seawater density, Mar. Geod. 35 (2012) 198–220.
[27] R. Tenzer, A. Abdalla, P. Vajda, The spherical harmonic representation of the gravitational field quantities generated by the ice density contrast, Contrib. Geophys. Geodes. 40 (3) (2010) 207–223.
[28] W. Chen, R. Tenzer, X. Gu, Sediment stripping correction to marine gravity data, Mar. Geod. 37 (4) (2014) 419–439.
[29] R. Tenzer, W. Chen, Mantle and sub-lithosphere mantle gravity maps from the LITHO1.0 global lithospheric model, Earth Sci. Rev. 194 (2019) 38–56.
[30] R. Tenzer, P. Vajda, Global atmospheric corrections to the gravity field quantities, Contrib. Geophys. Geodes. 39 (3) (2009) 221–236.
[31] R. Tenzer, Vajda P. Hamayun, Global maps of the step-wise topography corrected and crustal components stripped geoids using the CRUST2.0 model, Contrib. Geophys. Geodes. 39 (1) (2009) 1–18.
[32] R. Tenzer, Vajda P. Hamayun, A global correlation of the step-wise consolidated crust-stripped gravity field quantities with the topography, bathymetry, and the CRUST 2.0 Moho boundary, Contrib. Geophys. Geodes. 39 (2) (2009) 133–147.
[33] P. Novák, R. Tenzer, Gravitational gradients at satellite altitudes in global geophysical studies, Surv. Geophys. 34 (5) (2013) 653–673.
[34] G. Laske, G. Masters, Z. Ma, M.E. Pasyanos, Update on CRUST1.0-A 1-degree global model of Earth's crust, Geophys. Res. Abstr. 15 (2013) 2658.
[35] C.P. Conrad, C. Lithgow-Bertelloni, Influence of continental roots and asthenosphere on plate-mantle coupling, Geophys. Res. Lett. 33 (2006) L05312.
[36] R. Tenzer, W. Chen, Z. Ye, Empirical model of the gravitational field generated by the oceanic lithosphere, Adv. Space Res. 55 (1) (2015) 72–82.
[37] R. Tenzer, M. Bagherbandi, V. Gladkikh, Signature of the upper mantle density structure in the refined gravity data, Comput. Geosci. 16 (4) (2012) 975–986.
[38] R. Tenzer, W. Chen, S. Jin, Effect of the upper mantle density structure on the Moho geometry, Pure Appl. Geophys. 172 (6) (2015) 1563–1583.
[39] D.L. Turcotte, G. Schubert, Geodynamics, Second ed., Cambridge University Press, 2002, p. 472.
[40] Y. Fukao, M. Obayashi, Subducted slabs stagnant above, penetrating through, and trapped below the 660 km discontinuity, J. Geophys. Res.: Solid Earth 118 (11) (2013) 5920–5938.
[41] A. Ghosh, G. Thyagarajulu, B. Steinberger, The importance of upper mantle heterogeneity in generating the Indian Ocean Geoid Low, Geophys. Res. Lett. 44 (19) (2017) 9707–9715.
[42] F. Cammarano, S. Goes, P. Vacher, D. Giardini, Inferring upper-mantle temperatures from seismic velocities, Phys. Earth Planet. Inter. 138 (2003) 197–222.
[43] A. Forte, N.A. Simmons, S.P. Grand, Constraints on 3-D seismic models from global geodynamic observables: implications for the global mantle convective flow, in: G. Schubert (Ed.), Treatise of Geophysics, ., Elsevier, Burlington, MA, 2015, pp. 805–858, second ed.
[44] P. Moulik, G. Ekstrom, The relationships between large-scale variations in shear velocity, density, and compressional velocity in the Earth's mantle, J. Geophys. Rese. Solid Earth 121 (2016) 2737–2771.
[45] O. Čadek, L. Fleitout, A global geoid model with imposed plate velocities and partial layering, J. Geophys. Res. 104 (1999) 29055–29075.
[46] H. Nataf, Y. Ricard, 3SMAC: an a priori tomographic model of the upper mantle based on geophysical modeling, Phys. Earth Planet. Inter. 95 (1996) 101–122.
[47] N.A. Simmons, A.M. Forte, S.P. Grand, Thermochemical structure and dynamics of the African superplume, Geophys. Res. Lett. 34 (2007) L02301.
[48] J. Ritsema, A. Deuss, H.J. van Heijst, J.H. Woodhouse, S40RTS: a degree-40 shear-velocity model for the mantle from new Rayleigh wave dispersion, teleseismic traveltime and normal-mode splitting function measurements, Geophys. J. Int. 184 (2011) 1223–1236.
[49] C. Megnin, B. Romanowicz, The shear velocity structure of the mantle from the inversion of of body, surface and higher modes waveforms, Geophys. J. Int. 143 (2000) 709–728.
[50] S.W. French, B. Romanowicz, Whole-mantle radially anisotropic shear velocity structure from spectral-element waveform tomography, Geophys. J. Int. 199 (2014) 1303–1327.
[51] L. Auer, L. Boschi, T.W. Becker, T. Nissen-Meyer, D. Giardini, Savani: a variable-resolution whole-mantle model of anisotropic shear-velocity variations based on multiple datasets, J. Geophys. Rese. Solid Earth 119 (2014) 3006–3034.
[52] T.W. Becker, L. Boschi, A comparison of tomographic and geodynamic mantle models, Geochem. Geophys. Geosys. 3 (2002) 1003.
[53] N.A. Simmons, S.C. Myers, G. Johannesson, E. Matzel, S.P. Grand, Evidence for long-lived subduction of an ancient tectonic plate beneath the southern Indian Ocean, Geophys. Res. Lett. 42 (2015) 9270–9278.
[54] S.I. Karato, B.B. Karki, Origin of lateral variation of seismic wave velocities and density in the deep mantle, J. Geophys. Res. Solid Earth 106 (B10) (2001) 21771–21783.
[55] N.A. Simmons, A.M. Forte, S.P. Grand, Joint seismic, geodynamic and mineral physical constraints on three-dimensional mantle heterogeneity: implications for the relative importance of thermal versus compositional heterogeneity, Geophys. J. Int. 177 (5) (2009) 1284–1304.
[56] C. Adam, M. Yoshida, D. Suetsugu, T. Fakao, C. Cadio, Geodynamic modeling of the South Pacific superswell, Phys. Earth Planet. Inter. 229 (2014) 24–39.
[57] B.H. Hager, Subducted slabs and the geoid: constraints on mantle rheology and flow, J. Geophys. Res. 89 (1984) 6003–6015.
[58] F. Chambat, Y. Ricard, B. Valette, Flattening of the Earth: further from hydrostaticity than previously estimated, Geophys. J. Int. 183 (2010) 727–732.
[59] J.X. Mitrovica, A.M. Forte, A new inference of mantle viscosity based upon joint inversion of convection and glacial isostatic adjustment data, Earth Planet. Sci. Lett. 225 (1–2) (2004) 177–189.

Dr. Tenzer is the assistant professor in the Department of Land Surveying and Geo-Informatics at the Hong Kong Polytechnic University. He received MSc in Geodesy and Cartography (in 1995) and PhD in Physical Geodesy (in 1999) at the Slovak Technical University, as well as PhD in Satellite Geodesy (in 2008) at the Czech Technical University. Between 2001 and 2008, he held research positions at the University of New Brunswick, the University of Newcastle upon Tyne and the Delft University of Technology. Between 2009 and 2012, he taught at the University of Otago. Between 2012 and 2016, he was a visiting professor in the School of Geodesy and Geomatics at the Wuhan University. His research interests cover broad areas of Geodesy, Geophysics, Geodynamic and Planetary Science, with a major focus on geospatial modeling techniques and interpretations, theoretical geodesy and geophysics, geo-referencing, planetary inner structure and processes. He is the author of 4 books and more than 200 research journal articles (161 records on Scupus, 130 records on WoS). He presented his research in 195 conference contributions and 60 invited lectures at universities around the world. He is the member of editorial board and scientific adviser to several journals, while also contributing as the reviewer to more than 40 journals (including Nature Geoscience). Currently, he is the chair of the International Association of Geodesy (IAG) study group IC-SG7: Earth's inner structure from combined geophysical sources.